Available online at www.sciencedirect.com
SCIENCE DIRECT
Scripta Materialia 55 (2006) 29–33
Scripta MATERIALIA
www.actamat-journals.com

Viewpoint Paper

Nanoscale analysis of three-dimensional structures by electron tomography

M. Weyland,[a,b] T.J.V. Yates,[a] R.E. Dunin-Borkowski,[a] L. Laffont[a,c] and P.A. Midgley[a,*]

[a] *Department of Materials Science and Metallurgy, University of Cambridge, Pembroke Street, Cambridge CB2 3QZ, UK*
[b] *E13 Clark Hall, Department of Applied and Engineering Physics, Cornell University, Ithaca, NY 14853, USA*
[c] *LRCS, Universite de Picarde, 33 rue St Leu, 80039 Amiens Cedex, France*

Received 26 October 2005; accepted 20 December 2005
Available online 3 February 2006

Abstract—A significant challenge to the design of nanoscale materials and devices is the difficulty of characterising complex three-dimensional structures on small length scales. Electron tomography, a technique pioneered in the life sciences, has been developed for materials science by using high-angle annular dark-field scanning transmission electron microscopic tomography and energy filtered transmission electron microscopic tomography. We present tomographic analyses that reveal three very different types of information: the crystal habit of magnetite in magnetotactic bacteria, the morphology and composition of a silicon–germanium quantum dot, and compositional variations in iron–nickel nanoparticles. Both techniques are shown to return chemical and structural information that would be unattainable using conventional two-dimensional microscopy.

Keywords: Electron tomography; Scanning transmission electron microscopy (STEM); Energy filtered transmission electron microscopy (EFTEM); High angle annular dark field (HAADF); Nanostructure

1. Introduction

The transformation of promising nanoscience into practical nanotechnology relies on the detailed characterisation of complex nanostructures and devices. Conventional methods for materials characterisation are often of limited use and analysis in three dimensions is particularly challenging. Whilst a number of techniques, such as atomic force microscopy and conventional transmission electron microscopy (TEM), provide sufficient two-dimensional (2D) resolution, they have insufficient depth sensitivity to determine internal three-dimensional (3D) structure. One approach, devised in the late 1960s [1,2] for the 3D study of biological macromolecules, is electron tomography [3]. In electron tomography, an image signal must be a monotonic function of a physical property, the so-called 'projection requirement'. In the life sciences, bright-field images are recorded either from stained sections, in which amplitude contrast is dominant, or unstained sections, in which often phase contrast is used to delineate features. In materials science, bright-field images often contain unwanted diffraction contrast and Fresnel contrast that result from the strength and coherence of the scattering process and will lead to artefacts in the reconstruction. Instead, an incoherent TEM image may be formed either by collecting electrons that have been scattered to high angles inelastically, using high-angle annular dark-field scanning transmission electron microscopy (HAADF STEM) [4,5] or by energy filtered TEM (EFTEM) [6,7]. In this article, we illustrate the new types of information that such signals provide.

2. Experimental methods

2.1. Sample preparation

(i) Magnetotactic bacteria: Specimens of MV-1 magnetotactic bacteria were dried and dispersed on a holey carbon 200 mesh Cu grid. No staining was used.

(ii) Si–Ge quantum dots: A multi-period quantum dot (QD) structure was grown by gas source molecular

* Corresponding author. Tel.: +44 1223 334561; fax: +44 1223 334567; e-mail: pam33@cam.ac.uk

1359-6462/$ - see front matter © 2006 Acta Materialia Inc. Published by Elsevier Ltd. All rights reserved.
doi:10.1016/j.scriptamat.2005.12.058

beam epitaxy including two layers of buried dots and one uncapped layer. The QD sample was prepared for microscopy using standard cross sectional techniques, with final thinning carried out using a Gatan precision ion polishing system. The specimen was mounted in a Fischione model 2020 high tilt specimen holder and oriented in order to minimise shadowing of the surface dot from the bulk Si crystal during the tilt series.

(iii) Fe–Ni nanoparticles: Nanoparticles of 90Fe–10Ni composition were dispersed on 200 mesh Cu grids coated with holey carbon film. In order to minimise contamination, the specimen holder was plasma cleaned using a 10% oxygen–90% argon plasma [8] for 10 min, and then for a further 30 s with the specimen; this was then inserted immediately into the microscope.

2.2. HAADF STEM tomography

A 200 kV FEI Tecnai F20 field emission gun (FEG)-TEM, fitted with a SuperTWIN objective lens and a Fischione model 3000 HAADF detector, was optimised for medium resolution STEM to form a 0.4 nm probe at the specimen. STEM HAADF tilt series were undertaken either manually (tilting, tracking and re-focusing) or in automated fashion using the FEI eXplore3D acquisition software [9]. HAADF STEM images are formed by collecting scattered electrons using an annular detector [10,11]. With a sufficiently high collection angle (50 mrad was used here), the signal, formed primarily from unscreened elastic and quasi-elastic phonon scattered electrons, is approximately proportional to the specimen thickness and the square of the atomic number, Z. This, together with its relative insensitivity to diffraction conditions, makes STEM HAADF imaging ideal for electron tomography.

2.3. EFTEM tomography

Images formed using inelastic signals should also contain appropriate contrast for tomography as, to a first approximation, the intensity in an elemental (energy loss) map is linearly related to the concentration of the mapped elemental species. EFTEM has, since the availability of commercial in-column [12] and post column [13] energy filters, become a popular technique for rapid 2D mapping of inelastic scattering. Although electron energy loss spectroscopy (EELS) will provide excellent energy resolution, EELS mapping is relatively slow. Thus, for tomography, where rapid image acquisition leads to more comprehensive datasets, EFTEM is better suited [7].

An FEI Tecnai F20 FEGTEM, fitted with a Gatan imaging filter (GIF) 2000 with a 1k (1024×1024 pixel) CCD camera, was optimised for EFTEM by using a high beam current and an objective aperture of about 8 mrad for optimum spatial resolution [14]. During the tilt series acquisition, tracking and focusing were carried out manually. Digital Micrograph scripts [15] were used to automatically set energy loss offsets and for the acquisition of each energy loss image [16]. In order to compensate for energy loss drift, the zero-loss peak was checked every few tilt increments. In addition due to the changes in focus throughout the tilt series and/or possible misalignment of the projector optics the beam shift centring was also corrected throughout the series to ensure constant illumination conditions.

2.4. Tomographic reconstruction and visualization

All post processing of the datasets was carried out using procedures written in Interactive Data Language (IDL) V5.6. Tomographic alignment of the tilt series was carried out using a modified sequential cross-correlation method [17] to sub-pixel accuracy. The direction of the absolute tilt axis was fine-tuned by reconstruction of selected slices. Reconstruction was carried out using standard weighted backprojection methods and by multiplicative simultaneous iterative reconstruction technique (SIRT) [18] with 15–30 iterations. Voxel (volume pixel) projections and surface rendering of the reconstructions was generated using Amira V2.3.

3. Results

3.1. 3D morphology and nanometrology

Figure 1 illustrates the ability of electron tomography to reconstruct the morphology and internal architecture of nanostructures from a tilt series of STEM HAADF images, here recorded every 2° from −76° to +76°. The

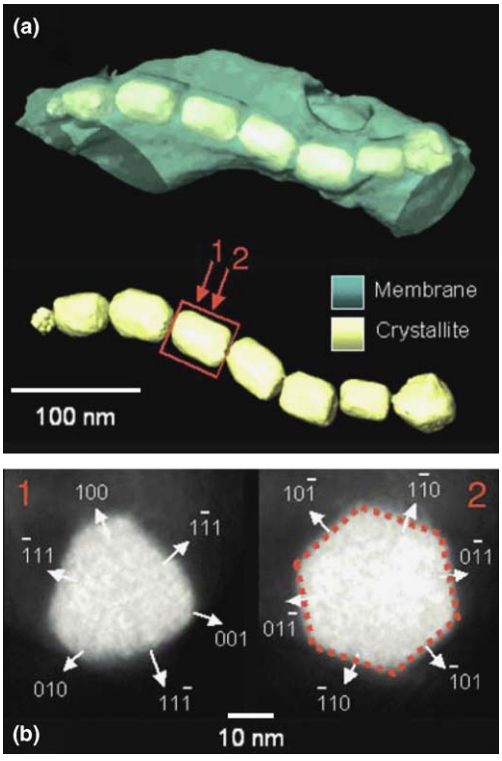

Figure 1. (a) A tomographic reconstruction of magnetotactic bacteria strain MV-1. The 'backbone' of magnetite crystals is evident. (b) Slices taken through a single magnetite crystal in the 'backbone' reveal the perfect crystal faceting of the cubic crystals, as revealed by the superposition of a regular hexagon (red dashes) on slice 2.

results are obtained from a single magnetotactic bacterial cell of strain MV-1 that contains a chain of 60×35 nm magnetite (Fe_3O_4) crystals. Such bacteria have been of interest in part because similar crystals were found in Martian meteorite ALH84001 [19]. Figure 1(a) shows a voxel projection of the tomographic reconstruction revealing the three-dimensional structure of the magnetite chain and an outline of the outer bacterial membrane. Figure 1(b) shows reconstructed slices taken from the end (labelled 1) and the centre (labelled 2) of a single crystallite. The perfection of the magnetite crystal is emphasised by the dotted regular hexagon. The ability to reconstruct the 3D internal architecture of nanoscale structures offers the possibility of using electron tomography for 3D nanoscale metrology. Such metrology is likely to be of great importance for the verification and calibration of nanoscale devices and structures in the future.

Quantum confinement structures have optical and electronic properties that are dominated by surface and interface states which may be combined with high strains and have very different properties from their bulk counterparts. The morphology and composition of such structures are key to understanding their unique properties. A total of 47 STEM HAADF images were acquired from an epitaxially grown silicon–germanium quantum dot (QD) with a tilt range of $\pm 70°$ and a 4° increment. Voxel (volume pixel) projections of the reconstruction along three major axes (Fig. 2(a)) show the reconstruction of an uncapped (surface) dot and a buried dot, 60 nm below the surface. The reconstruction also reveals that sample preparation had led to the loss of

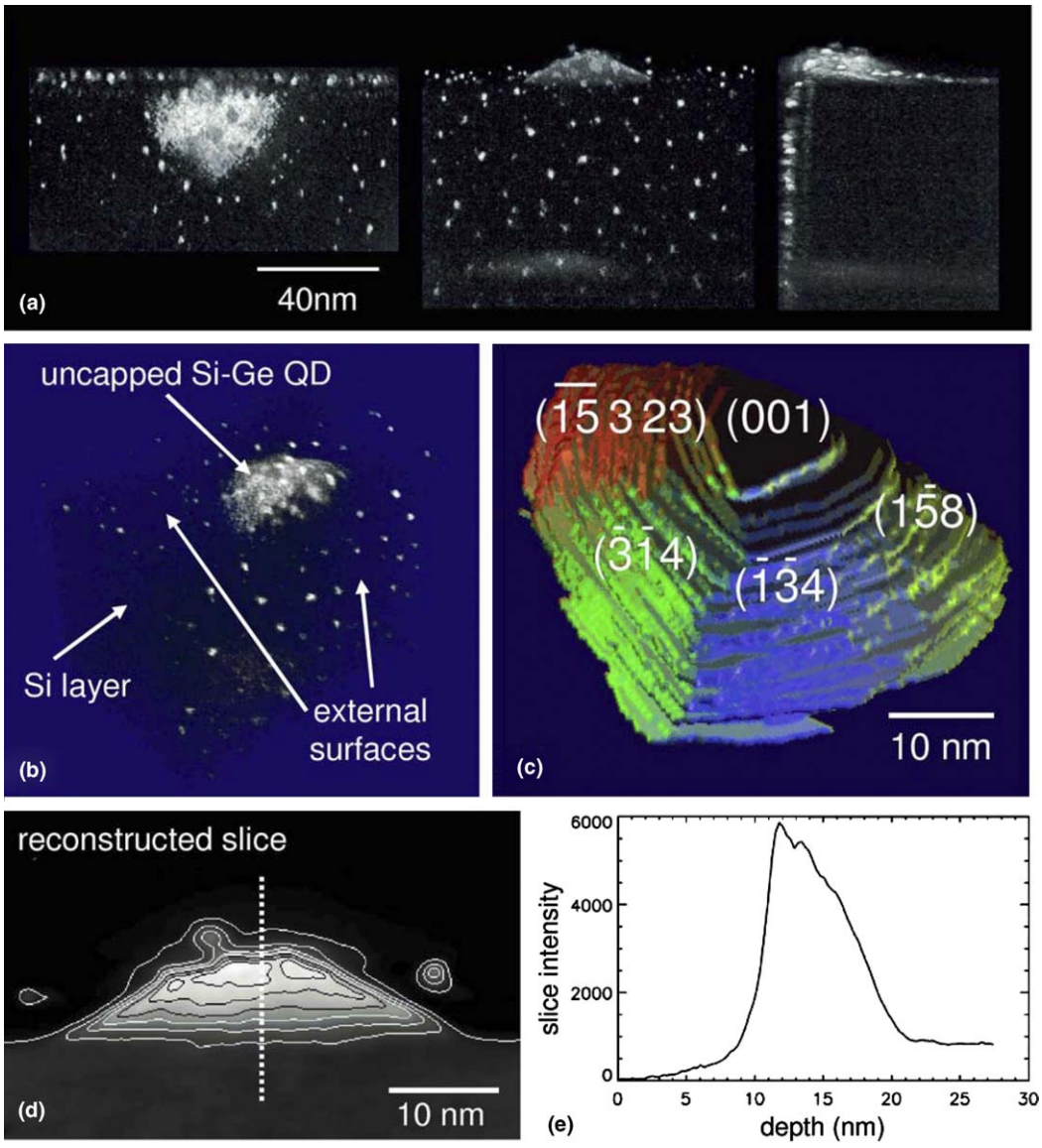

Figure 2. Quantum dot reconstruction. (a) Montage of projections parallel to three mutually perpendicular crystallographic axes. (b) Voxel (volume pixel) projections of the reconstructed volume. (c) Segmented iso-surface render revealing the shape of surface dot. The lighting directions have been chosen at normals to the exposed facets. A smooth change in colour will arise from a rounded surface and an abrupt change in colour indicates a sharp change in the surface angle. (d) Contour plot overlaid on the image from slice through dot, averaged over 5 pixels. (e) Line plot averaged from a 5×5 pixel "core" through dot at dashed line in (d).

approximately half the dot and the presence of small surface contaminants (see Fig. 2(b)). Although unwanted, they serve to mark the outer surfaces of the specimen that would otherwise be almost invisible.

The shape of the surface dot can be visualised using a surface render of the reconstruction volume, as shown in Figure 2(c). The major facets have been tentatively indexed, based on their angle to the (0 0 1) growth surface and coupled with knowledge of the likely facets expected for this size of dot in the silicon–germanium system. As the shape of the dot in projection is initially unknown, no conclusions can be drawn about variations in composition from individual HAADF STEM images. In the reconstruction, this uncertainty is removed, and the intensity in each voxel can, in principle, be related to the local average atomic number. A five-voxel averaged slice of the surface dot (Fig. 2(d) and (e)) shows an unambiguous increase in intensity at the top of the dot, with the surface apparently richer in germanium. However, due to the complexity of high-angle scattering for crystalline specimens, a true compositional profile cannot be determined without further calculation (or calibration).

3.2. 3D compositional mapping

In order to demonstrate EFTEM tomography, a multiple-element analysis of a specimen of cryogenically evaporated iron–nickel nanoparticles was performed. These spherical super-paramagnetic particles, with diameters ranging from 10 to 100 nm, have been characterised previously by conventional 2D EFTEM and electron holography [20]. Here we answer two outstanding questions using tomographic analysis: what is the dominant metal in the oxide and whether the oxide coating forms before, or after, particle agglomeration.

The area chosen for acquisition is shown in the BF image of Figure 3(a). At each increment, nine energy loss images were acquired, three for each of the iron (650 eV, 680 eV and 730 eV), nickel (800 eV, 830 eV and 880 eV) and oxygen edges (485 eV, 515 eV and 555 eV). For all acquisitions a slit width of 10 eV, an acquisition time of 10 s and a 2× binning (to yield 512 pixel × 512 pixel images) was used. The acquisition consisted of a total of 36 increments, at 4° steps from −76° to 64°. The total acquisition time for all 324 images was just over two hours.

After acquisition, two pre-edge images and one post-edge image were spatially aligned to correct for drift between acquisitions. Elemental maps were generated using a standard three-window technique [14]. The resultant iron and oxygen map series were aligned to the respective nickel map in order to match the registration for the following tomographic alignment. Alignment was carried out on the nickel map tilt series, as this series had the highest signal to noise ratio (SNR), and reconstruction of the three series was carried out using multiplicative SIRT.

Average projected elemental maps from the three sampled elements are shown in Figure 3(a). These show enhanced SNR when compared to the conventional elemental maps (shown directly above the summed maps), as expected from the polytropic montage effect [21]. A combined red–green–blue (RGB) voxel projection of these elemental volumes is shown in Figure 3(b). In

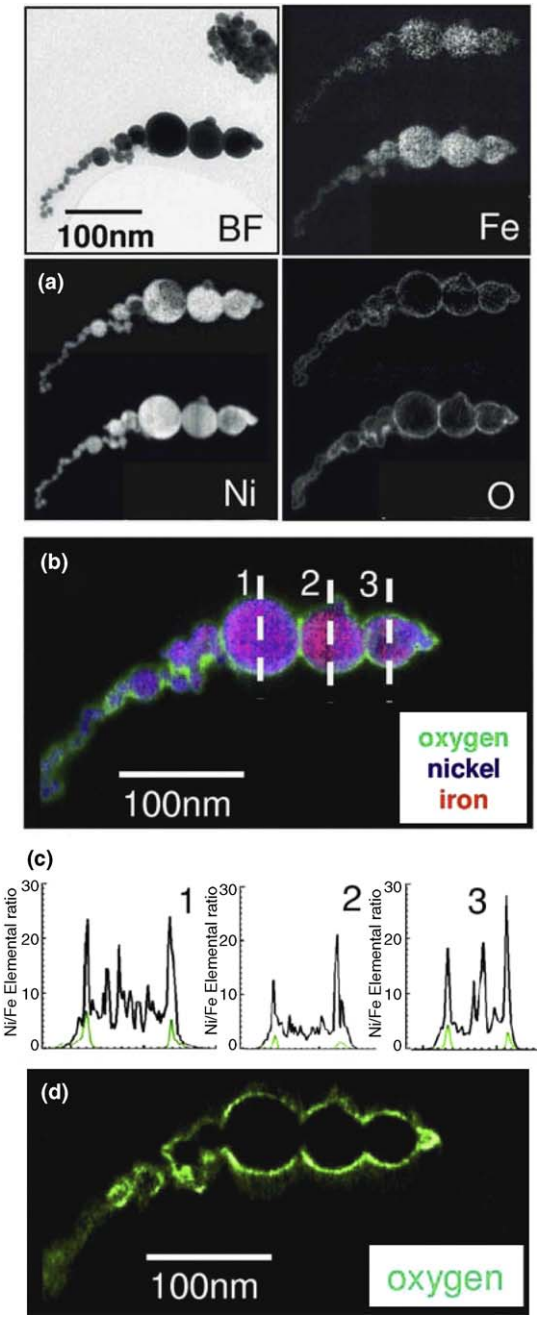

Figure 3. (a) Zero loss bright-field image and two-dimensional elemental maps of nickel, iron and oxygen recorded from a chain of FeNi nanoparticles chosen for EFTEM tomography acquisition. The lower elemental maps are generated by re-projecting the tomographic reconstructions in the zero tilt direction. The upper elemental maps are the equivalent raw conventional elemental maps. (b) RGB voxel (volume pixel) projection of the combined reconstructions of the FeNi nanoparticles. (c) Three "core samples" have been extracted from the central volume of the three largest particles (marked 1, 2 and 3, respectively, in (b)). The "core samples" have been averaged in the two shorter dimensions to give average line traces of all three elements. Plotted for all three samples are the nickel/iron ratios (black) and the equivalent oxygen line traces (green). (d) A slice through the oxygen tomographic reconstruction showing how the oxide covers the ensemble of nanoparticles rather than individual nanoparticles.

order to determine the chemical nature of the surface oxide, sub-volumes ('core samples') have been taken from the centre of each of the three largest nanoparticles. The data in this sub-volume has been summed to give a single line trace for each element. Plotted in Figure 3(c) is the ratio of the nickel to iron signals for each of the three particles and the corresponding oxygen signal. Despite the high level of noise, there is a clear increase in the nickel content at the edges of each particle. This increase corresponds, in each nanoparticle, exactly with the position of the surface oxide as indicated by the oxygen trace.

Two-dimensional elemental maps of the oxygen signal, such as in Figure 3(b), suggest that the oxide coating extends between the nanoparticles. However in order to image this directly a slice can be taken through the oxygen reconstruction at the centre of the nanoparticle chain, Figure 3(d), revealing the interior structure where the nanoparticles join. This slice clearly shows a gap in the oxide coating and confirms that the particles sintered together before the oxide formed, a conclusion impossible to draw using only conventional 2D imaging.

4. Conclusions

Electron tomography using HAADF STEM and EF-TEM can recover information that would be lost during conventional 2D microscopy. The ability to section and analyse volumetric data post facto allows for a more complete understanding of nanoscale systems. Such techniques will become invaluable as nanostructured systems become increasingly complex and difficult to visualise using conventional methodologies.

Acknowledgements

The authors wish to acknowledge the financial support of the EPSRC, the Royal Commission for the Exhibition of 1851, the Royal Society, the Isaac Newton Trust and FEI Company. The authors wish to thank Diana Zhi for preparing the Si–Ge quantum dot specimen, Martin Hÿtch and Ryan Chong for providing the Fe–Ni nanoparticle specimen and Richard Frankel, Denis Bazylinski, Peter Buseck and Bertrand Devouard for the culture and provision of the MV-1 magnetotactic bacteria. We thank Sir John Meurig Thomas for his continuing support.

References

[1] W. Hoppe, R. Langer, G. Knesch, C. Poppe, Naturwissenschaften 55 (1968) 333.
[2] D.J. De Rosier, A. Klug, Nature 217 (1968) 130.
[3] A.J. Koster, R. Grimm, D. Typke, R. Hegerl, A. Stoschek, J. Walz, et al., J. Struct. Biol. 120 (1997) 276.
[4] P.A. Midgley, M. Weyland, J.M. Thomas, B.F.G. Johnson, Chem. Commun. (2001) 907.
[5] P.A. Midgley, M. Weyland, Ultramicroscopy 96 (2003) 413.
[6] G. Möbus, B.J. Inkson, Appl. Phys. Lett. 79 (2001) 1369.
[7] M. Weyland, P.A. Midgley, Microsc. Microanal. 9 (2003) 542.
[8] T.C. Isabell, P.E. Fischione, C. O'Keefe, M.U. Guruz, V.P. Dravid, Microsc. Microanal. 5 (1999) 126.
[9] FEI Company, Eindhoven, Netherlands.
[10] A. Howie, J. Microsc. 117 (1979) 11.
[11] J.M. Thomas, P.A. Midgley, T.J.V. Yates, J.S. Barnard, R. Raja, I. Arslan, et al., Angew. Chem. Int. Ed. 43 (2004) 6745.
[12] J. Mayer, in: G.W. Bailey, J. Bentley, J.A. Small (Eds.), 50th Annual Meeting of the Electron Microscopy Society of America, San Francisco Press Inc., San Francisco, CA, 1992, p. 1198.
[13] O.L. Krivanek, A.J. Gubbens, M.K. Kundmannn, G.C. Carpenter, in: Proc. 51st Annual Meeting of the Microscopy Society of America, San Francisco Press Inc, San Francisco, CA, 1993, p. 586.
[14] R.F. Egerton, Electron Energy-Loss Spectroscopy in the Electron Microscope, Plenum Press, New York, NY, 1996.
[15] P.J. Thomas, P.A. Midgley, Ultramicroscopy 88 (2001) 179.
[16] P.A. Midgley, P.J. Thomas, Topics Catal. 21 (2002) 109.
[17] R. Guckenberger, Ultramicroscopy 9 (1982) 167.
[18] P. Gilbert, J. Theoret. Biol. 36 (1972) 105.
[19] D.S. McKay, E.K. Gibson Jr., K.L. Thomas-Keprta, H. Vali, C.S. Romanek, S.J. Clemett, et al., Science 273 (1996) 924.
[20] M.J. Hytch, R.E. Dunin-Borkowski, M.R. Scheinfien, J. Moulin, C. Duhamel, F. Mazaleyrat, et al., Phys. Rev. Lett. 91 (2003) 257207.
[21] R.G. Hart, Science 159 (1968) 1464.